

# Space–Time Variations of the Shear Wave Attenuation Field in the Upper Mantle of Seismic and Low Seismicity Areas

Yu. F. Kopnichev<sup>a</sup>, D. D. Gordienko<sup>b</sup>, and I. N. Sokolova<sup>b</sup>

<sup>a</sup> *Institute of Physics of the Earth, Russian Academy of Sciences, 123995 Russia*

<sup>b</sup> *Institute of Geophysical Research, National Nuclear Center of Republic of Kazakhstan, Alma-Ata, 050020 Kazakhstan*

Received April 16, 2007

**Abstract**—This paper deals with characteristics of the short period *S*-wave attenuation field in the rupture zones of 37 large and great earthquakes with  $M_s = 7.0$ – $8.6$ , as well as in low seismicity areas. We estimate the effective quality factor from *Sn* and *Lg* coda envelopes in two time intervals ( $Q_1$  and  $Q_2$ ). The quantity  $Q_1$  is a measure of shear wave attenuation in the uppermost mantle, at depths of down to approximately 200–250 km, while  $Q_2$  is relevant to deeper horizons of the upper mantle. We studied variations in the attenuation field in the rupture zone of the 1950 Assam earthquake. We examined the parameters  $Q_1$ ,  $Q_2$ , and  $Q_1/Q_2$  as functions of the time  $\Delta T$  elapsed after a large earthquake. It is shown that the parameter  $Q_2$  in rupture zones is practically independent of  $\Delta T$ , while the quantities  $Q_1$  and  $Q_1/Q_2$  increase until  $\Delta T \sim 20$ – $25$  years, especially rapidly for normal, normal-oblique, and strike-slip earthquake mechanisms. This analysis provides evidence that, as  $\Delta T$  increases, so does the quality factor in the upper mantle for shear waves. It is supposed that this is related to the rise of mantle fluids to the crust. Geodynamic mechanisms are discussed that can support a comparatively rapid “drying” of the upper mantle beneath earthquake rupture zones.

**DOI:** 10.1134/S0742046309010059

## INTRODUCTION

It was shown in [10, 12] that the attenuation of short period *S* waves significantly varied over time in the rupture zones of large Tien Shan earthquakes. Large crustal earthquakes are followed by a gradually increasing effective  $Q_s$  in the upper mantle (down to a depth of about 200 km) with a concurrent diminution of  $Q_s$  in the lower crust. These results were obtained for reverse-faulting and reverse-oblique earthquakes that are typical of Tien Shan [10, 12].

The present study considers space–time variations in the *S*-wave attenuation field in the rupture zones of 37 large and great earthquakes occurring in various regions worldwide ( $M_s$  magnitudes between 7.0 and 8.6). Special attention is paid to comparison of characteristics of the attenuation field for events with different types of faulting. For comparison purposes we also study the variations of effective quality factor in those regions where no large ( $M \geq 6.5$ ) earthquakes have occurred since 1900.

## THE DATA

We used over 400 seismograms of shallow earthquakes ( $h \leq 40$  km) recorded by 46 digital and analog stations. The bulk of these records came from digital GSN stations [24]. The other data include records made at stations of the Complex Seismological Expedition (Institute of Physics of the Earth, Russian Academy of

Sciences), the Institute of Geophysical Research, National Nuclear Center, Republic of Kazakhstan, as well as by the Kirgizian network KNET (Tables 1, 2).

The seismograms we are concerned with here were recorded at distances of  $\sim 300$ – $600$  km from the rupture zones of 37 earthquakes with  $M_s = 7.0$ – $8.6$  and depths shallower than 60 km in various regions worldwide, primarily in Central and East Asia, North, Central, and South Americas (Table 1, Figs. 1, 2). Almost half of these events (18) occurred in Benioff zones, 15 in Central Asia (Tien Shan, Altai, Mongolia, Tibet, and the Himalayas), 3 in the western US, and 1 in Turkey. The distribution over the focal mechanisms is as follows: 7 normal and normal-oblique events, 8 strike-slip, 15 reverse and thrusting mechanisms, and 7 reverse-oblique. For comparison purposes we also examined records made at the same distances in those regions where no large ( $M \geq 6.5$ ) events have occurred since 1900 (Table 2).

Variations in the attenuation field are best seen at frequencies of about 1 Hz [7, 22, 37]; accordingly, we did a preliminary frequency filtering with a filter centered at 1.25 Hz and with a bandwidth of  $2/3$  octaves at 0.7 of the maximum, similar to the corresponding ChISS (frequency selective) filter [4].

**Table 1.** The values of  $Q_1$  and  $Q_2$  for different rupture zones

| Region        | Date        | $\varphi^\circ$ | $\lambda^\circ$ | $M_s$ | Faulting type   | $Q_1$ | $Q_2$ | Station |
|---------------|-------------|-----------------|-----------------|-------|-----------------|-------|-------|---------|
| Himalayas     | 12 Jun 1897 | 26              | 91              | 7.8   | thrust          | 200   | 310   | LSA     |
| Tien Shan     | 22 Aug 1902 | 39.8            | 76.2            | 7.6   | reverse         | 590   | 790   | TLG     |
| Himalayas     | 4 Apr 1905  | 42.8            | 77.3            | 7.7   | reverse         | 670   | 790   | MAKZ    |
| Tien Shan     | 3 Jan 11    | 33.0            | 76.00           | 7.4   | thrust          | 390   | 530   | NIL     |
| Tibet         | 16 Dec 20   | 36.62           | 105.40          | 8.4   | reverse-oblique | 740   | 420   | XAN     |
| Altai         | 10 Aug 31   | 47.00           | 90.06           | 7.7   | strike-slip     | 420   | 540   | MKAR    |
| Japan         | 2 Mar 33    | 39.75           | 144.5           | 8.3   | normal          | 1300  | 1150  | ERM     |
| Himalayas     | 15 Jan 34   | 27.55           | 87.09           | 8.1   | thrust          | 330   | 510   | LSA     |
| Indonesia     | 28 Dec 35   | 0.00            | 98.25           | 7.5   | strike-slip     | 270   | 270   | BTDF    |
| Japan         | 7 Dec 44    | 33.75           | 136.00          | 7.8   | thrust          | 300   | 390   | MAJO    |
| Himalayas     | 15 Aug 50   | 28.38           | 96.76           | 8.6   | strike-slip     | 790   | 340   | LSA     |
| California    | 21 Jul 52   | 35.00           | -119.00         | 7.8   | reverse-oblique | 410   | 300   | MNV     |
| Kamchatka     | 4 Nov 52    | 52.75           | 159.50          | 8.2   | thrust          | 290   | 410   | PET     |
| Japan         | 25 Nov 53   | 34.00           | 141.50          | 7.9   | normal          | 1100  | 440   | MAJO    |
| Baikal region | 27 Jun 57   | 56.20           | 116.59          | 7.6   | normal-oblique  | 1700  | 710   | BDN     |
| Mongolia      | 4 Dec 57    | 45.31           | 99.21           | 8.0   | reverse-oblique | 540   | 740   | ULN     |
| Nevada        | 18 Aug 59   | 44.70           | -110.80         | 7.5   | normal          | 540   | 570   | DUG     |
| Chile         | 22 May 60   | -43.40          | -75.50          | 8.5   | thrust          | 340   | 510   | PLCA    |
| Alaska        | 28 Mar 64   | 61.10           | -147.60         | 8.4   | thrust          | 310   | 360   | COLA    |
| Chile         | 28 Dec 66   | -25.50          | -70.70          | 7.7   | thrust          | 250   | 370   | LCO     |
| Tien Shan     | 11 Aug 74   | 39.39           | 73.86           | 7.2   | reverse-oblique | 350   | 420   | GAR     |
| Indonesia     | 19 Aug 77   | -11.09          | 118.46          | 8.1   | normal          | 1300  | 410   | KAPI    |
| Tien Shan     | 24 Mar 78   | 42.9            | 78.70           | 7.0   | reverse-oblique | 490   | 740   | MAKZ    |
| Chile         | 3 Mar 85    | -33.13          | -71.87          | 7.8   | thrust          | 290   | 490   | LCO     |
| Mexico        | 19 Sep 85   | 18.14           | -102.71         | 8.1   | thrust          | 200   | 350   | UNM     |
| California    | 28 Jun 92   | 34.18           | -116.51         | 7.6   | strike-slip     | 380   | 310   | MNV     |
| Tien Shan     | 19 Aug 92   | 42.10           | 73.60           | 7.3   | reverse         | 270   | 630   | AML     |
| Kuril Is.     | 4 Oct 94    | 43.77           | 147.32          | 8.3   | reverse-oblique | 200   | 530   | ERM     |
| Indonesia     | 1 Jan 96    | 0.73            | 119.93          | 7.9   | reverse-oblique | 260   | 510   | KAPI    |
| Tibet         | 8 Nov 97    | 35.07           | 87.32           | 7.9   | strike-slip     | 120   | 320   | LSA     |
| Kamchatka     | 5 Dec 97    | 54.84           | 162.04          | 7.6   | reverse         | 210   | 420   | PET     |
| Turkey        | 17 Aug 99   | 40.75           | 29.86           | 7.7   | strike-slip     | 200   | 370   | ANTO    |
| Salvador      | 13 Jan 01   | 13.05           | -98.66          | 7.8   | normal          | 120   | 330   | JTS     |
| Mexico        | 30 Sep 99   | 16.6            | -96.93          | 7.5   | normal          | 220   | 320   | UNM     |
| Peru          | 23 Jun 01   | -16.26          | -73.64          | 8.2   | thrust          | 150   | 360   | NNA     |
| Alaska        | 3 Nov 02    | 63.52           | -147.44         | 7.9   | strike-slip     | 310   | 390   | COLA    |
| Altai         | 27 Sep 03   | 50.04           | 87.81           | 7.3   | strike-slip     | 290   | 740   | MKAR    |

**Table 2.** The values of  $Q_1$ ,  $Q_2$ , and  $Q_1/Q_2$  for low seismicity areas

| Region                 | Station | $Q_1$ | $Q_2$ | $Q_1/Q_2$ |
|------------------------|---------|-------|-------|-----------|
| Eastern Alps           | BFO     | 260   | 590   | 0.44      |
| Kopet Dag              | VAN     | 240   | 510   | 0.47      |
| Northern Kazakhstan    | ABKAR   | 340   | 590   | 0.58      |
| Eastern Kazakhstan     | KURK    | 540   | 840   | 0.64      |
| Western Tien Shan      | KKAR    | 270   | 520   | 0.52      |
| Northern Tien Shan*    | AAK     | 300   | 540   | 0.56      |
| Northern Tien Shan*    | CHM     | 260   | 620   | 0.42      |
| Northern Tien Shan*    | EKS2    | 260   | 670   | 0.39      |
| Northern Tien Shan*    | KBK     | 270   | 770   | 0.35      |
| Northern Tien Shan*    | KZA     | 290   | 670   | 0.43      |
| Northern Tien Shan*    | TKM2    | 310   | 740   | 0.42      |
| Northern Tien Shan*    | UCH     | 200   | 700   | 0.29      |
| Northern Tien Shan*    | ULHL    | 330   | 600   | 0.55      |
| Northern Tien Shan*    | USP     | 280   | 700   | 0.40      |
| Northern Tien Shan*    | MKAR    | 270   | 790   | 0.34      |
| Northern Tien Shan**   | AAK     | 390   | 740   | 0.53      |
| Northern Tien Shan**   | CHM     | 300   | 670   | 0.45      |
| Northern Tien Shan**   | EKS2    | 290   | 630   | 0.46      |
| Northern Tien Shan**   | KBK     | 270   | 770   | 0.35      |
| Northern Tien Shan**   | KZA     | 240   | 790   | 0.30      |
| Northern Tien Shan**   | TKM2    | 390   | 740   | 0.53      |
| Northern Tien Shan**   | UCH     | 240   | 600   | 0.40      |
| Northern Tien Shan**   | ULHL    | 390   | 740   | 0.53      |
| Northern Tien Shan**   | USP     | 300   | 680   | 0.44      |
| Northern Tien Shan     | KKAR    | 250   | 900   | 0.28      |
| Central Tien Shan      | KKAR    | 370   | 720   | 0.51      |
| Central Tien Shan      | TLG     | 310   | 720   | 0.43      |
| Southern Tien Shan     | CHM     | 350   | 770   | 0.45      |
| Southern Tien Shan     | TKM2    | 260   | 790   | 0.33      |
| Southern Tien Shan     | TKM2    | 260   | 970   | 0.27      |
| Eastern Tien Shan      | MAKZ    | 330   | 720   | 0.46      |
| Eastern Tien Shan      | WMQ     | 240   | 540   | 0.44      |
| Eastern Tien Shan      | MAKZ    | 380   | 700   | 0.54      |
| Pakistan               | NIL     | 240   | 400   | 0.60      |
| Northern Baikal region | TLY     | 280   | 510   | 0.55      |
| Central Baikal region  | TLY     | 470   | 970   | 0.48      |
| Mongolia               | ULN     | 250   | 740   | 0.34      |
| Central Tibet          | LSA     | 140   | 350   | 0.40      |
| Southern Tibet         | LSA     | 190   | 490   | 0.39      |
| South Africa           | LPTB    | 590   | 1050  | 0.56      |
| South Africa           | SUR     | 540   | 1270  | 0.43      |
| Australia              | NWAO    | 690   | 1700  | 0.41      |
| Kamchatka              | PET     | 230   | 440   | 0.52      |
| San Andreas, US        | GLA     | 220   | 290   | 0.76      |
| San Andreas, US        | MNV     | 210   | 390   | 0.54      |
| New Madrid, US         | MYNC    | 370   | 870   | 0.43      |

Notes: \* Aftershocks of the magnitude 6.0 December 1, 2003 earthquake.

\*\* Aftershocks of the magnitude 6.1 February 14, 2005 earthquake.

## THE METHOD

We considered envelopes of  $Lg$  and  $Sn$  codas on records of comparatively small earthquakes (generally with  $M < 5.5$ ). The crustal  $Lg$  phase is a combination of shear waves reflected from crustal discontinuities at overcritical angles; its average velocity is very stable over different regions and is close to 3.5 km/s [5, 7, 8]. The  $Lg$  phase disappears if even part of the path traverses the oceanic crust and also if the attenuation in the continental crust is strong enough. In such cases the records contain the  $Sn$  group alone, which penetrates into the upper mantle, followed by its coda (Fig. 3) [8].

Several works [5, 7, 8, 22] report on comprehensive studies of coda characteristics at frequencies around 1 Hz (including the analysis of arrival directions and apparent velocities, polarization, space–time variations, and so on). It was concluded from this analysis that the codas of  $Sn$  and  $Lg$  are of similar origin, being primarily composed of shear waves reflected from numerous subhorizontal discontinuities in the upper mantle. Figure 3 shows three components in the record of a shallow ( $h = 30$  km) event from the rupture zone of the great 1933 Sanriku-Oki earthquake made at the ERM station. It can be seen that the coda at 1.25 Hz is dominated by horizontal components at times of about 3 min after the arrival of  $Sn$ , which corroborates the conclusion reached in [5, 7, 8, 22].

As the time  $t$  elapsed since the start of earthquake radiation increases, the coda begins to contain waves that are incident at the Moho at increasingly greater angles and penetrate to increasingly greater depths in the upper mantle. Figure 4 shows a simplified diagram of rays that make up the coda of  $Sn$  and  $Lg$ . The ray I is the head wave that propagates along the Moho. Later arrivals consist of  $S$  waves reflected from various upper mantle discontinuities. If there is a zone of relatively low (high) attenuation in a rupture zone in the upper mantle, this will lead to a relatively slow (fast) attenuation of amplitude in the initial part of the coda (rays II and III). Ray III is followed by  $S$  waves penetrating into the region of “normal” (for the depth range considered) attenuation. This provides a corresponding rapid increase or decrease in the rate of amplitude attenuation in the coda.

We used the formula  $A_c(t) \sim \exp(-\pi t/Q_s T)/t$  ( $T$  is the period of oscillations [7]) to find the effective  $Q$  in two time intervals, the first being 70 s immediately after  $Lg$  (from  $t = 110$ – $180$  s at epicentral distances  $\Delta \sim 300$  km to  $t = 180$ – $250$  s at  $\Delta \sim 600$  km) and the second being  $t = 250$ – $400$  s (we shall denote the respective quantities as  $Q_1$  and  $Q_2$  for brevity). When no 1-Hz  $Lg$  group was present in a record, measurements were made after the time specified in the relevant travel time table.

We are going to estimate the depth of ray penetration  $h_r$  by the  $Lg$  coda in a simple two-layered model: a crust 50 km thick and an upper mantle with an average  $S$  velocity of 3.5 and 4.6 km/s, respectively. Table 3 lists values of  $h_r$  for two values of ray shift  $l_r$  in the upper

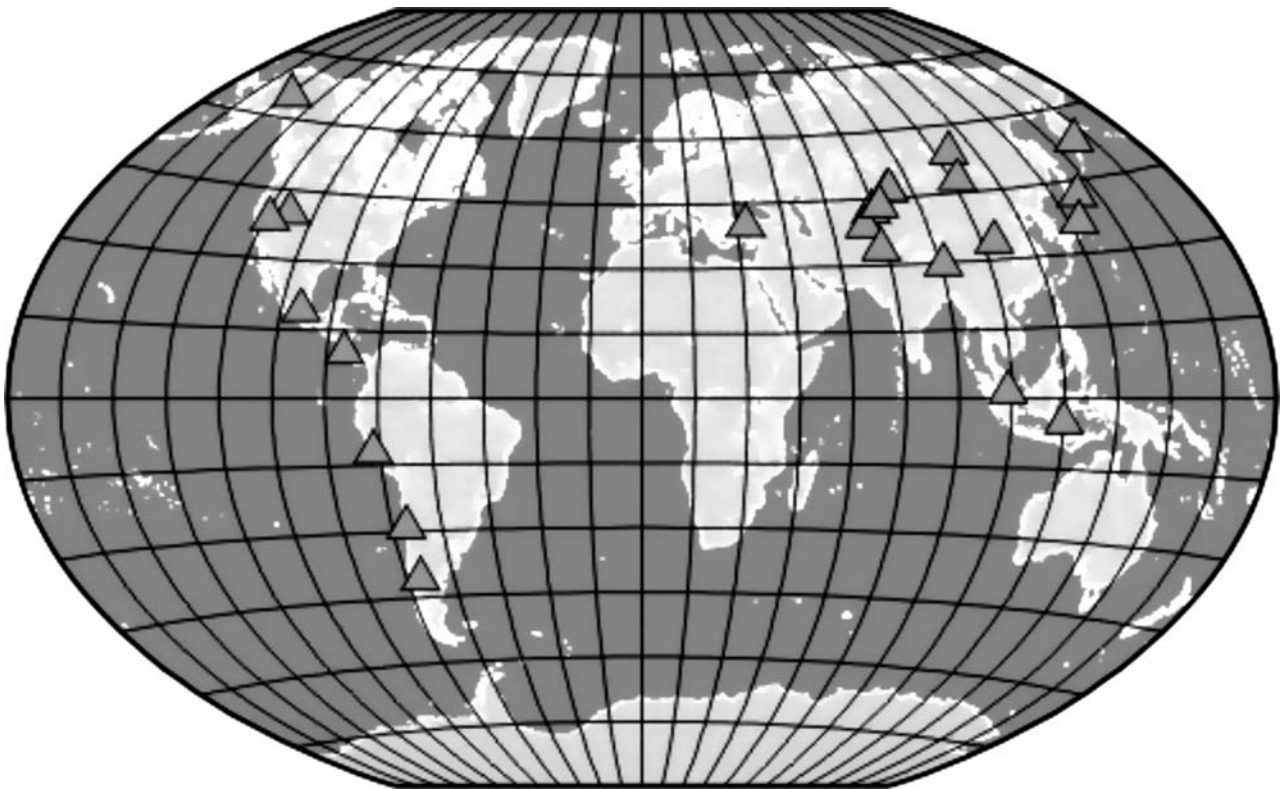


**Fig. 1.** Positions of seismic stations whose records were used to study the attenuation field in the rupture zones of large earthquakes.

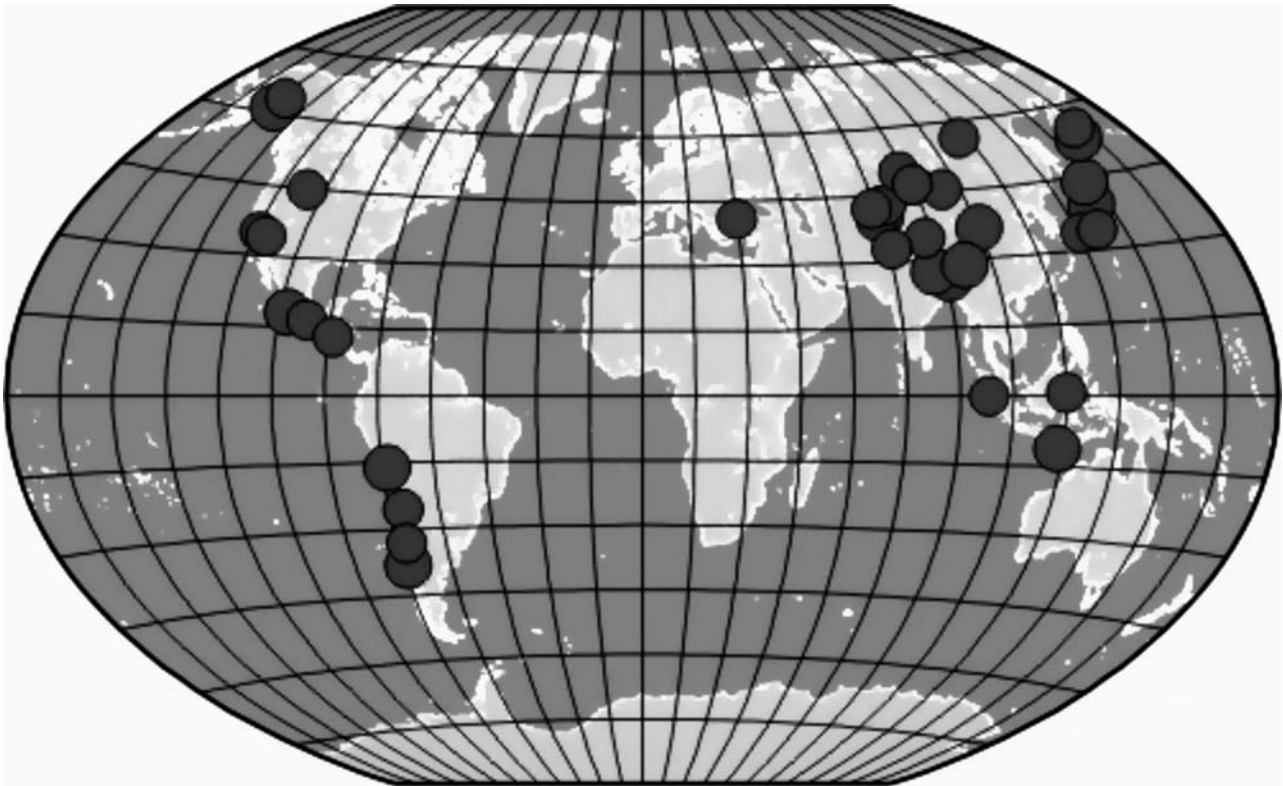


**Fig. 2.** Epicenters of large and great earthquakes. Smaller symbols stand for  $7.0 \leq M_s < 8.0$  events, larger ones for  $M_s \geq 8.0$ .

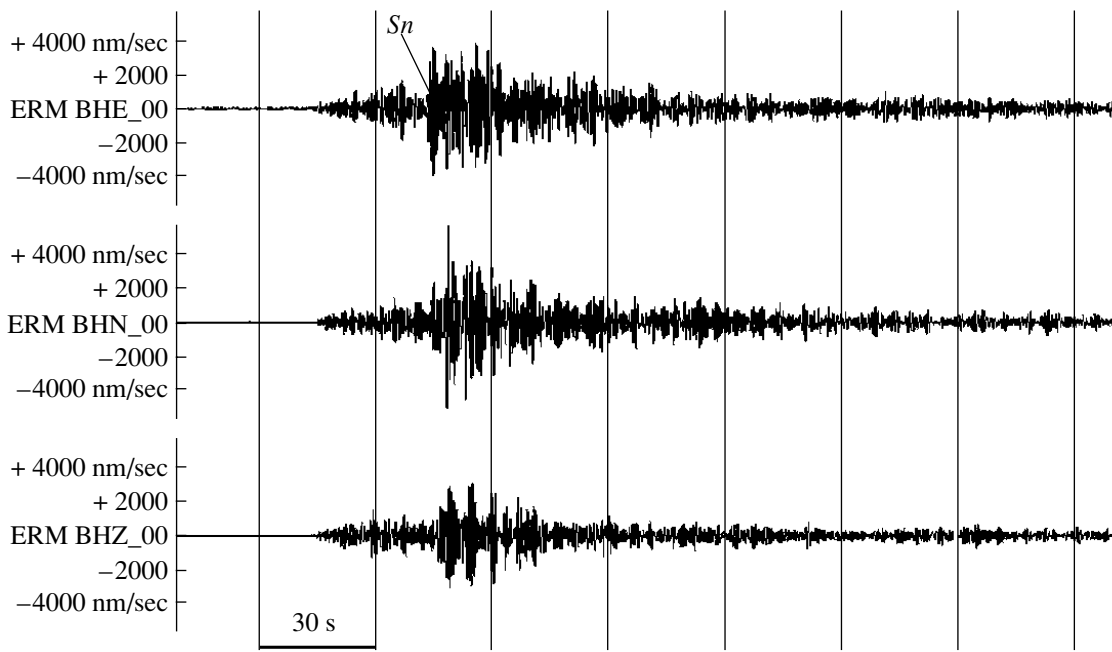


**Fig. 3.** Record of an earthquake emanating from the rupture zone of the Sanriku-Oki earthquake (Table 1). June 16, 1999, 39.54° N, 144.70° E,  $h = 30$  km. The ERM station, the 1.25 Hz channel.

mantle (50 and 100 km) with zero focal depth for different epicentral distances (300 to 600 km).

It follows from this table that, assuming  $l_r = 50$  km for the range of epicentral distances of interest, the rays will penetrate to the depth  $\sim 90$ –135 km, with the figure being 170–255 km for  $l_r = 100$  km. Naturally, these crude estimates should be viewed as just a first approximation.

#### DATA ANALYSIS

We begin by examining the background variations of coda characteristics and effective  $Q$  in those regions

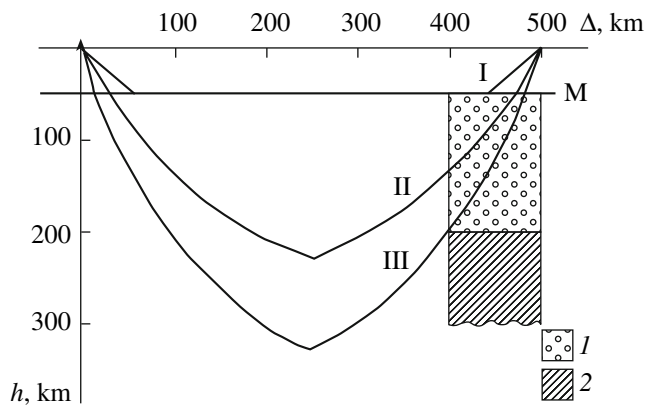


**Fig. 4.** Ray diagram illustrating the generation of  $Lg$  and  $Sn$  codas: (1) the region of the upper mantle where attenuation varies over time, (2) region of “normal” attenuation.

where no  $M \geq 6.5$  earthquakes have occurred since 1900.

**Coda Envelope Variations in Regions with No Large Earthquakes since 1900.** We analyzed earthquake records made at 29 seismic stations in various regions of the world, primarily in Central Asia. Data for a total of 46 paths were used (Table 2). It follows from the table that  $Q_1$  and  $Q_2$  varied in the ranges 140–690 and 290–1700, respectively. Lower values of  $Q_1$  (140–230) were observed in the anomalous zone of northern Tien Shan identified in [11, 14, 16], in central and southern Tibet, in a volcanic area of Kamchatka, and in a creep zone on the San Andreas fault in central California [23]. Intermediate values of  $Q_1$  (240–390) were obtained for the Eastern Alps, certain areas in Kopet Dag, the Kazakh Platform, many areas of Tien Shan, certain areas of Pakistan and Mongolia (east of the 1957 Gobi Altai earthquake rupture zone), the northern Baikal region, and the North American Platform (New Madrid). High values of  $Q_1$  (470–690) were recorded in areas of northern Kazakhstan, the central Baikal region, and ancient platforms (South Africa and Australia).

The lower values of  $Q_2$  (290–510) were observed in Kopet Dag, Pakistan, central and southern Tibet, central California, and Kamchatka. Intermediate values (520–900) are typical of the Eastern Alps, certain areas in the Kazakh Platform, Tien Shan, Mongolia, and the New Madrid area. Lastly, very high values (970–1700) were observed for certain areas in southern Tien Shan (the TKM2 station), the central Baikal region, and platform areas.

Figure 5 shows a correlative relation between  $Q_1$  and  $Q_2$ . One has a linear dependence:  $Q_1 = 0.36Q_2 + 59.33$ , the correlation coefficient is equal to 0.79. The ratio  $Q_1/Q_2$  in the continental areas considered varies in the range 0.27–0.76, with the mean being  $0.45 \pm 0.10$ .

It is of interest to examine large deviations of  $Q_1/Q_2$  from the mean value. From Table 2 it follows that very low values of  $Q_1/Q_2$  (0.27–0.34) are observed in the anomalous zone of northern Tien Shan, as well as in Mongolia. Very high values of  $Q_1/Q_2$ , outside the  $3\sigma$  range (0.76), occur in the creep zone of the San Andreas fault.

We can get an idea of the spatial variations in the coda amplitude attenuation rate by examining characteristics of records for events occurring in the rupture zone of the 1950 Assam earthquake and the environs.

**Variations of the Attenuation Field in the Assam Rupture Zone.** The great Assam earthquake of August 15, 1950 ( $M_w = 8.6$ ) was the largest tectonic event in intracontinental areas and the greatest earthquake outside the subduction zones for the last 105 years [25, 39]. Triep and Sykes [39] believe that this event is related to significant changes in seismicity over the entire Asian continent. Below we examine the variation in the attenuation field of short period shear waves in a large area of the Himalayas and southern Tibet that includes the rupture zone in question.

We processed digital records of crustal earthquakes with  $M \sim 4.0$ – $5.5$  made at the LSA and KMI stations during the period 1987–2004 (Fig. 6). We analyzed a total of over 70 seismograms recorded in the range of epicentral distance  $\sim 300$ – $600$  km.

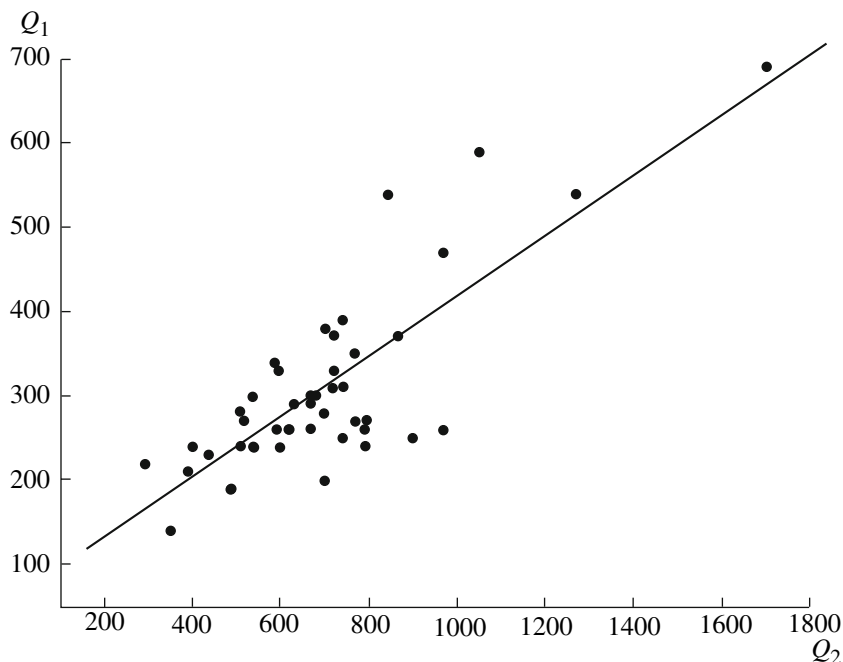
**Table 3.** Estimates of the depth to which rays penetrate in the upper mantle

| $\Delta$ , km | 300 |     | 600 |     |
|---------------|-----|-----|-----|-----|
| $t$ , s       | 180 |     | 250 |     |
| $l_r$ , km    | 50  | 100 | 50  | 100 |
| $h_r$ , km    | 135 | 255 | 90  | 170 |

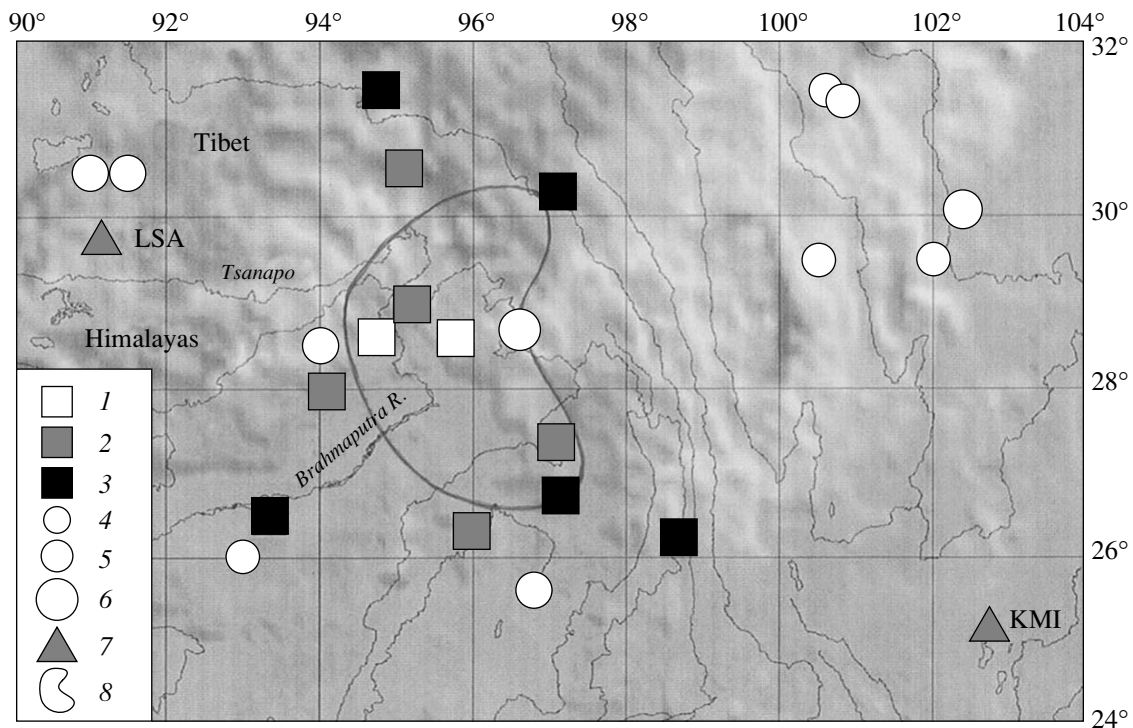
Figure 7 shows sample records of two earthquakes, one in the rupture zone and the other north of that zone. The epicenters of both events were at approximately equal distances from the LSA station (390–400 km). It is seen from this figure that the coda is attenuating much slower in the rupture zone during the time interval of about 70 s after  $Lg$ .

Figure 8 presents envelopes of the  $Lg$  coda constructed for different areas in the rupture zone and its environs based on records of the LSA station. The envelopes are seen to have significantly different shapes. Overall, the  $Lg$  coda falls off at a slower rate in its initial segment in the rupture zone compared with the area around the zone. The envelope shape variations for more distant codas are much less noticeable.

It follows from Table 4 that the values of  $Q_1$  and  $Q_2$  vary from 470 to 790 and from 340 to 380, respectively, within the rupture zone, the respective ranges being 190 to 490 and 320 to 490 for its environs. The parameter  $Q_1/Q_2$  varies within 1.19–2.32 within the rupture zone and from 0.50 to 1.21 outside it. We note that the values



**Fig. 5.** Correlative relationship between  $Q_1$  and  $Q_2$  for low seismicity areas.



**Fig. 6.** Map of the study area. Values of  $Q_1/Q_2$ : (1)  $> 2.00$ , 2 – 0.90–1.25, 3 – 0.50–0.85. Epicenters of large earthquakes: (4)  $7.0 \leq M < 7.5$ , (5)  $7.5 \leq M \leq 8.0$ , (6)  $M = 8.6$ ; (7) seismic stations, (8) aftershock area of the Assam earthquake [25].

of  $Q_1/Q_2$  in the aftershock area are within  $(7-19)\sigma$  for the mean value and the standard deviation  $\sigma$  obtained in areas of low seismicity for the last 100 years. It is interesting to note that the greatest values of  $Q_1/Q_2$  correspond to the “bend” region of the rupture zone, where the aftershock area changes its trend from northeast to southeast. Significantly higher values of that parameter (0.69–1.21) are also observed for the environs of the rupture zone (at distances of approximately 100 km from the aftershock area). At the same time, the values

of  $Q_1/Q_2$  at distances of ~100–200 km north of the zone are decreasing down to the “normal” level (~0.50) relevant to the areas of low seismicity. At the southeastern boundary of the rupture zone (based on data recorded at KMI),  $Q_1/Q_2$  is only slightly above the mean level (0.66), and decreases further away from the boundary (at a distance of 150 km), down to 0.53. It should be noted that the highest values of  $Q_1/Q_2$  outside of the rupture zone occur near the northwestern, western, and southern boundaries of that zone. It is of interest to

**Table 4.** The values of  $Q_1$ ,  $Q_2$  and  $Q_1/Q_2$  in the rupture zone of the Assam earthquake and its environs

| Area no. | $\varphi^\circ$ , N | $\lambda^\circ$ , E | $Q_1$ | $Q_2$ | $Q_1/Q_2$ | Station |
|----------|---------------------|---------------------|-------|-------|-----------|---------|
| 1        | 25.9–26.7           | 95.5–96.5           | 410   | 340   | 1.21      | LSA     |
| 2        | 26.1–26.8           | 93.0–93.7           | 310   | 370   | 0.84      | LSA     |
| 3        | 27.1–27.6           | 96.8–97.4           | 440   | 370   | 1.19      | LSA     |
| 4        | 27.7–28.2           | 93.3–94.3           | 340   | 360   | 0.94      | LSA     |
| 5        | 28.3–28.9           | 95.4–96.1           | 740   | 340   | 2.18      | LSA     |
| 6        | 28.2–29.02          | 94.4–95.1           | 790   | 340   | 2.32      | LSA     |
| 7        | 28.6–29.3           | 95.0–95.3           | 470   | 380   | 1.24      | LSA     |
| 8        | 30.3–30.5           | 96.8–97.4           | 240   | 350   | 0.69      | LSA     |
| 9        | 30.3–31.0           | 94.7–95.5           | 490   | 430   | 1.14      | LSA     |
| 10       | 31.0–31.9           | 94.1–95.5           | 210   | 420   | 0.50      | LSA     |
| 11       | 26.0–26.1           | 98.7–98.9           | 190   | 360   | 0.53      | KMI     |
| 12       | 26.6–26.9           | 97.0–97.2           | 210   | 320   | 0.66      | KMI     |

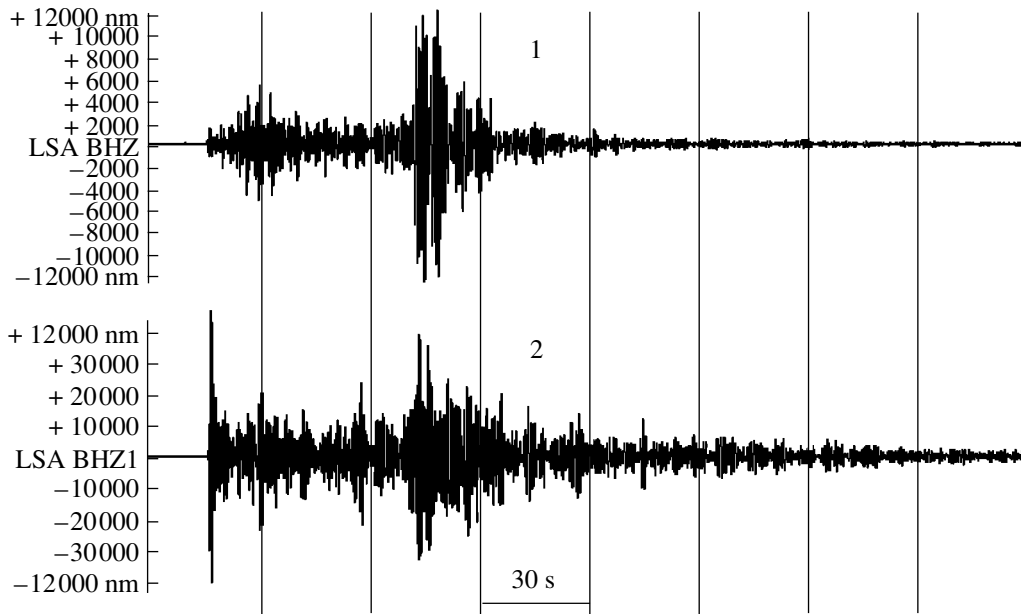


**Fig. 7.** Sample seismograms recorded at the LSA station (vertical component, the 1.25 Hz filter): (1) August 5, 2000, 31.85°N, 94.43° E,  $h = 33$  km (north of the rupture zone), (2) November 30, 2002, 28.62° N, 95.07° E,  $h = 31$  km (central part of the rupture zone).

point out that the epicenters of the largest earthquakes, which occurred within about 350 km from the rupture zone boundary since 1900, are west and south of the rupture zone ( $M_s = 7.0$ – $8.0$ , Fig. 6).

It can thus be said that the rupture zone of the Assam earthquake shows significant variations in the attenuation field ~40–55 years after the event. Overall, the rupture zone shows very high values of  $Q_1$  and  $Q_1/Q_2$  compared with the normal values for low seismicity areas. As well, the area of increased values for those parameters is appreciably greater than the rupture zone.

The worldwide network of digital stations (GSN) began operation comparatively recently; therefore, in order to investigate variations in the attenuation field in rupture zones over spans of tens of years we used a special approach, analyzing seismic information for a great number of rupture zones of large and great earthquakes worldwide having different delay times  $\Delta T$  after the events.

**Integral Characteristics of the Attenuation Field in the Rupture Zones of Large and Great Earthquakes of the World.** Figure 9 shows sample seismograms of comparatively small events occurring in the rupture zones of two great earthquakes, namely, the 1933 Sanriku-Oki and the 1994 Shikotan events, both with  $M = 8.3$ . Their respective focal mechanisms were normal and reverse-oblique. Both these events were recorded by the same station with nearly identical epicentral distances (350–360 km). Nevertheless, the coda following the first of these events was decaying much more slowly than for the second, over approximately three minutes after the  $S_n$  wave train.

Figure 10 presents examples of coda envelopes for earthquakes occurring comparatively soon ( $\Delta T$  below 5 years) after four large earthquakes: 2001 Salvador, 2003 Altai, 1994 Shikotan, and 2001 Peru. The earthquakes had different types of faulting: normal, strike-slip, reverse-oblique, and thrusting mechanisms. It follows from this figure that all the envelopes contain an interval of relatively higher slope in the initial segment of the coda. The slope is much smaller in the interval 250–400 s. A completely different pattern was observed in those regions where the events were considered that occurred after comparatively long intervals of time after large and great earthquakes. Figure 11 shows examples of coda envelopes for the rupture zones of four other large earthquakes (for  $\Delta T = 17$ – $96$  years): the 1957 Muya (normal-oblique faulting), the Assam (strike-slip), the 1902 Kashgar (reverse-slip), and the 1934 Himalayan (thrusting mechanism). It can be seen that all these cases show a much slower amplitude attenuation in the earlier part of the coda than is the case in Fig. 10, especially slow coda attenuation being observed for normal-oblique and strike-slip faulting mechanisms.

Coda envelope characteristics were considered for the rupture zones of 37 earthquakes occurring in different regions worldwide. In those cases where several types of coda envelope were identified in the rupture zone (as is the case for the Assam earthquake), for the sake of definiteness we selected that envelope having the greatest value of  $Q_1$ . It follows from Table 1 and Fig. 12 that the values of  $Q_1$  for the different rupture zones vary in the range 120–1700, while the variation of  $Q_2$  is much smaller, between 270 and 1150.

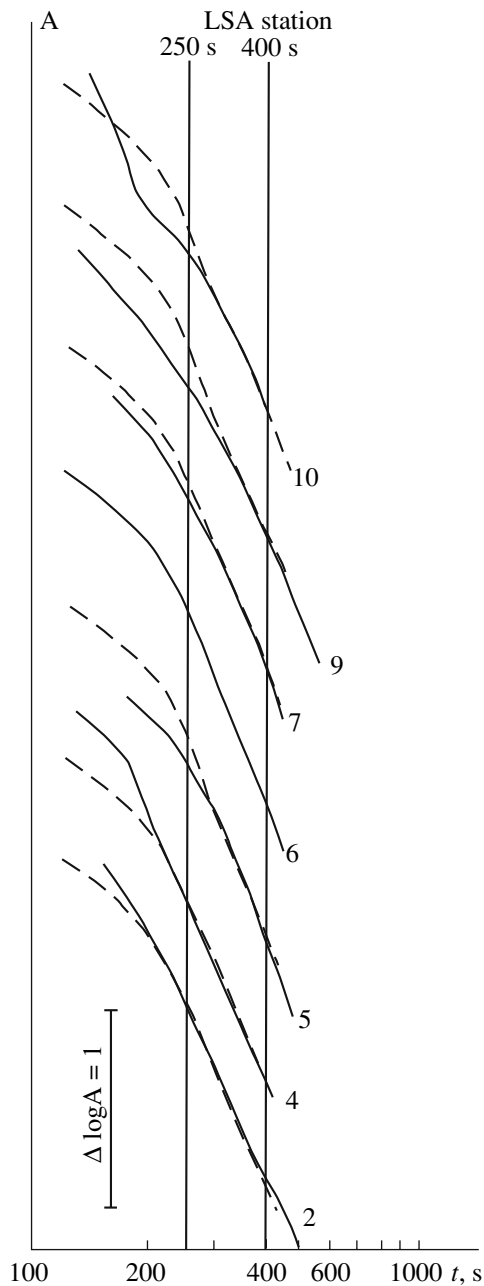


**Fig. 8.** Coda envelopes for different parts of the rupture zone and its environs (the LSA station). Numerals refer to areas concerned (Table 4). (5, 6, and 7) are data for the rupture zone, (2, 4, 9, and 10) are outside the zone. Dashed lines represent the envelope for area 6.

We again divided all the data relating to  $Q_1$  and  $Q_2$  into three sets corresponding to increased, intermediate, and lower attenuation.

The lowest values of  $Q_1$  (120–290) were observed for eleven earthquakes of the mostly thrusting type of slip in different regions of the Benioff zone, as well as for five events having thrusting, reverse-slip, and strike-slip mechanisms in Central and West Asia occurring in 1897, 1992, 1997, 1999, and 2003. The intermediate

values of  $Q_1$  (300–700) were due to twelve earthquakes having different types of faulting in Central Asia and North America (outside the Benioff zone), as well as to three thrusting events in the Benioff zone. Lastly, the highest values of  $Q_1$  (700–1700) were obtained only for six earthquakes having normal, normal-oblique, strike-slip, and reverse-oblique mechanisms occurring in Central Asia and in the Benioff zone. Characteristically, this set of events does not contain earthquakes with reverse and thrusting faulting.

There is also a well-pronounced dependence of the maximum values of  $Q_1$  on slip type. The highest values of  $Q_1$  were obtained for normal and normal-oblique types (up to 1100–1700), up to 740–790 for strike-slip and reverse-oblique mechanisms, up to 590–670 for reverse faulting, and up to 330–390 for thrusting mechanisms.

The numbers of earthquakes with different values of  $Q_2$  are very disproportionate (Fig. 13). The greatest number of events (20) falls in the increased attenuation set ( $Q_2 = 270$ –420), with eleven being in the Benioff zone and nine in other regions. We note that the overwhelming number of such events (16) occurred at boundaries of major lithosphere plates or their environs and two more occurred in Tibet, which has a very strong attenuation in the upper mantle [30].

The intermediate attenuation set ( $Q_2 = 440$ –630) contains ten earthquakes (five in the Benioff zone). Lastly, the lower attenuation set ( $Q_2 = 710$ –1150) contains only seven events, with six being in Central Asia. We note that each set contains earthquakes with different types of slip.

The foregoing analysis shows that the variation in  $Q_1$  is primarily controlled by the focal mechanism, while  $Q_2$  largely by the geographic position of the area of study.

Figure 12 shows the values of  $Q_1$  plotted against the time  $\Delta T$ . It is seen that the earlier aftershocks of large earthquakes ( $\Delta T \leq 1$  yr) yield very low values of  $Q_1$ . Except for the zone of the 2003 Altai earthquake, these values do not exceed 150, i.e., are situated at the lower boundary of the data scatter band for the low seismicity areas or even below it. As  $\Delta T$  increases, the  $Q$  does so too (over 20–25 years), with the rate of increase being much higher for normal and strike-slip events than for reverse and thrusting mechanisms. The highest values of  $Q_1$  stray beyond the limits of the band corresponding to the low seismicity areas. When  $\Delta T > 35$  years, the values of  $Q_1$  for normal and strike-slip events begin to show a general decrease, while those for reverse and thrusting mechanisms, as well as for reverse-oblique events, persist at the same level (the slightly higher values of  $Q_1$  for two reverse and one reverse-oblique events in Central Asia for  $\Delta T > 75$  years may be related to regional features of the attenuation field). We note that in all cases for  $\Delta T > 2$  yr, the values of  $Q_1$  do not fall below 200, i.e., are certainly above the mean value that corresponds to  $\Delta T < 1$  yr.

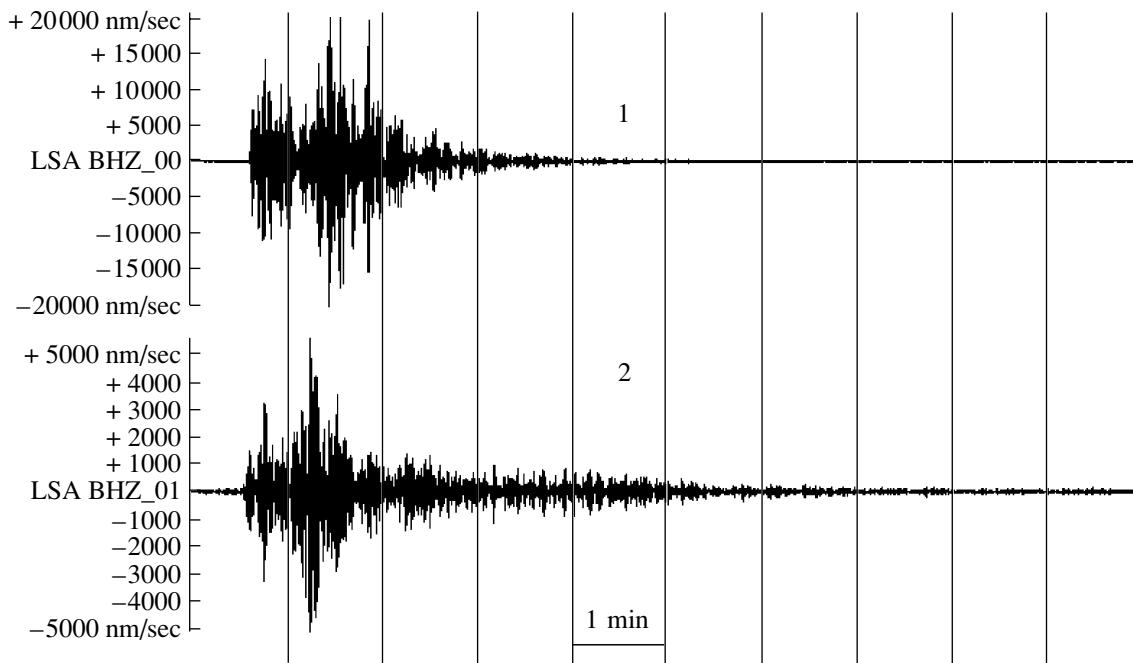


**Fig. 9.** Sample seismograms of shallow earthquakes emanating from two rupture zones: (1) 1994 Shikotan earthquake rupture zone, April 22, 1998, 43.45° N, 147.04° E,  $h = 43$  km, (2) 1933 Sanriku-Oki earthquake rupture zone, September 17, 1995, 38.97° N, 144.41° E,  $h = 33$  km. The ERM station, the 1.25 Hz channel.

Figure 13 illustrates the  $Q_2$  vs.  $\Delta T$  relationship. In this case for  $\Delta T < 1$  yr, the values of  $Q_2$  are mostly below 400 (the only exception is the 2003 Altai earthquake, with this region being characterized by a lower average attenuation in the upper mantle [9, 21]). However, the parameter  $Q_2$  is almost independent of time in the present case. Overall, nearly 97% of all data fall into the band corresponding to the low seismicity areas, the maximum values of that parameter being significantly below the upper boundary of the band. We note that the values of  $Q_2$  are practically independent of slip type here. The highest value of  $Q_2$  (1150) is for the Sanriku-Oki earthquake, which is the greatest normal-slip event to have occurred on our planet in the last 100 years [34].

We sought to minimize the effects of attenuation variations in different tectonic regions by again considering the values of  $Q_1$  normalized by  $Q_2$  (the parameter  $Q_1/Q_2$ ). Figure 14 shows  $Q_1/Q_2$  as a function of time  $\Delta T$ . As in the previous treatment, the earthquakes were divided into four sets by slip type. The  $\pm \sigma$  band is plotted as obtained previously for the low seismicity areas (the last 100 years). It can be seen that the values of  $Q_1/Q_2$  for the aftershocks occurring within the first year (mostly within the first few months) after large earthquakes are within that band. For larger  $\Delta T$  one notes a sharp difference between the values of that parameter for different slip types. For normal and strike-slip displacements the values of  $Q_1/Q_2$  increased very fast over 20–25 years, reaching 2.4–3.2, which is far beyond the  $15 \sigma$  range. For  $\Delta T > 25$  years one notices a falloff of the mean  $Q_1/Q_2$  for these slip types. For reverse and

thrusting mechanisms, this parameter is increasing at a much slower rate, varying in a comparatively narrow range (0.65–0.86) (within  $(2-4)\sigma$ ) for  $\Delta T > 25$  years. The values of  $Q_1/Q_2$  for reverse-oblique mechanisms are intermediate between “pure” reverse and strike-slip events.

We note that the increase in  $Q_1/Q_2$  is primarily due to the rapid increase in  $Q_1$  (Table 1). The greatest values occur for the rupture zones of the following earthquakes: the Chinese earthquake, the Assam, the Muya, and the Boso-Oki, for which we also got very high values of  $Q_1$  (740–1700).

Figure 15 shows  $Q_1/Q_2$  plotted against magnitude. (We selected data for reverse and thrusting mechanisms with  $\Delta T > 12$  years and for the other types of slip with  $\Delta T > 6$  years). It is seen that the parameter in question is increasing rather rapidly with increasing magnitude for fourteen events having normal, normal-oblique, strike-slip, and reverse-oblique mechanisms, with the correlation coefficient being 0.56. For earthquakes having reverse and thrusting types of slip, the values of  $Q_1/Q_2$  are nearly independent of the magnitude.

## DISCUSSION OF RESULTS

We note first that one ordinarily (outside the rupture zones) has  $Q_1/Q_2 < 0.50$  on the average. This provides evidence of a significant decrease in the upper mantle attenuation of  $S$  waves with increasing depth, which is consistent with the available data on the overall characteristics of the upper mantle quality factor derived by a

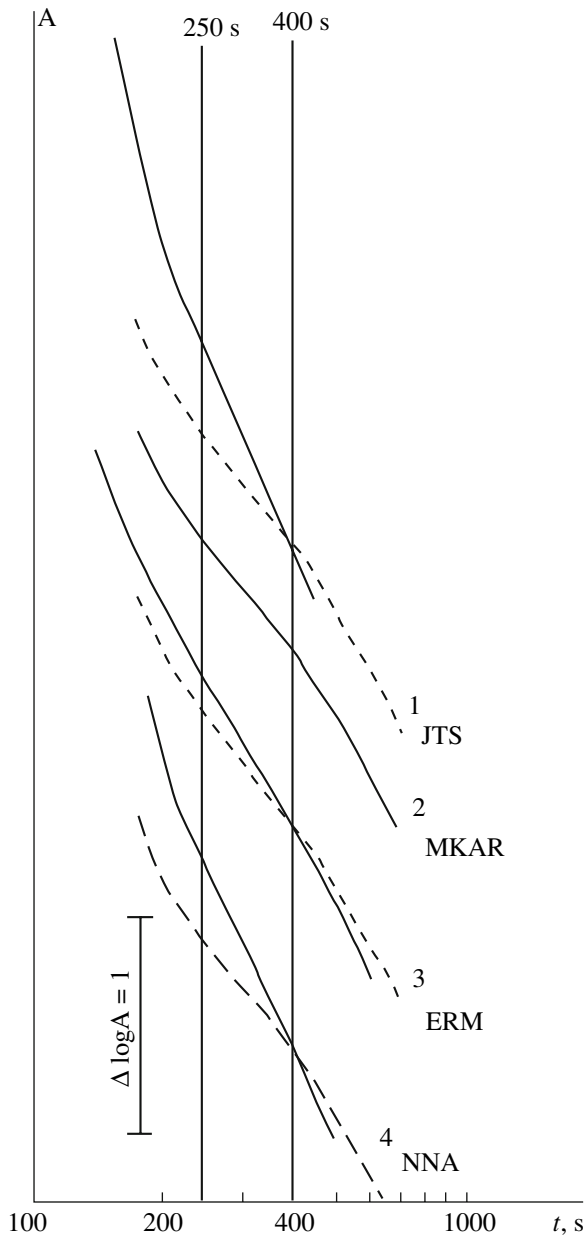


**Fig. 10.** Envelopes from records of aftershocks and earthquakes occurring within an interval  $\Delta T$  equal to 5 years after large earthquakes: (1) 2001 Salvador (normal faulting), (2) 2003 Altai (strike-slip), (3) 1994 Shikotan I., Kurils (reverse-oblique), (4) 2001 Peru (thrust). Dashed lines show the envelope for the Altai earthquake. JTS, MKAR, ERM, and NNA are station designations.

variety of methods [7, 8, 21, 22]. Overall, low values of  $Q_1$  and  $Q_2$  are observed in Tibet and the Alpine belt, which exhibit increased shear wave attenuation [8, 21, 30]. At the same time, high values of these parameters are recorded for certain areas of ancient crust in Central Asia, for which lower upper mantle attenuation has been detected [9, 21]. There are significant variations in the parameters even within one and the same tectonic province (e.g., Tien Shan or the Baikal Rift Zone). A

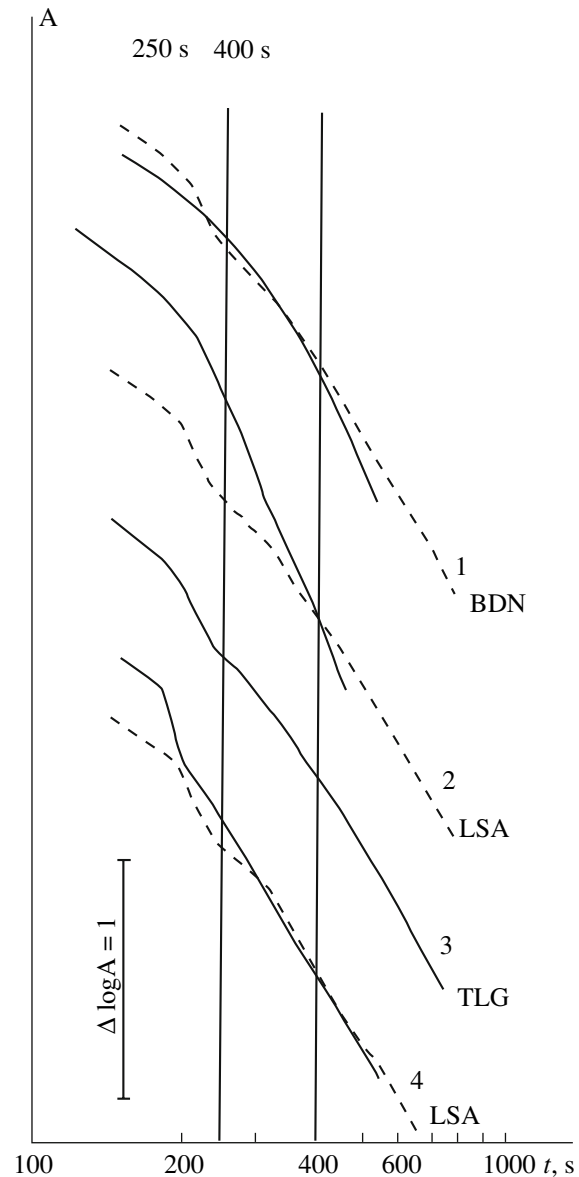


**Fig. 11.** Envelopes for records of local earthquakes occurring in the rupture zones of large and great earthquakes with intervals  $\Delta T$  greater than 17 years: (1) 1957 Muya, Baikal region (normal-oblique), (2) 1950 Assam, Himalayas (strike-slip), (3) 1902 Kashgar, Tien Shan (reverse), (4) 1934 Bihar-Nepal, Himalayas (thrust). Dashed lines represent the envelope for the Kashgar earthquake. BDN, LSA, and TLG are station designations.

more detailed investigation of this problem is outside the scope of the present paper.

We now consider the factors that give rise to time-dependent variations of the attenuation field structure in rupture zones. It should first be noted that coda characteristics can in principle vary owing to changes in the seismic wave velocity field (e.g., due to focusing and defocusing effects). But in the first place, it is difficult to expect that these effects can cause similar changes in the

rate of decay of coda amplitudes over comparatively long intervals of time. Secondly, results of numerical modeling show that the influence of attenuation changes in the crust and upper mantle on the wave pattern is much greater than that of velocity changes [6].

It follows from Table 1 and Figs. 12–14 that the rupture zone of a large earthquake has very low values of  $Q_1$  and  $Q_1/Q_2$ , as well as roughly “normal” values of  $Q_2$  during the first year after the event. This corresponds to high attenuation of  $S$  waves in the upper mantle (according to our estimates, down to depths of about 200–250 km).

The values of  $Q_1$  gradually increase over time until  $\Delta T \sim 20$ –25 years. The increase is best seen in the variations of  $Q_1/Q_2$ , for which local features of the attenuation field related to its spatial variation have been largely removed [7, 21, 22, 37]. The increase of these quantities is due to decreased  $S$  wave attenuation in the upper mantle. (We wish to point out that the increased attenuation in the crust may also have a certain effect, because, as is seen from Fig. 4, the waves that make up the  $Lg$  coda travel over increasingly shorter paths as time goes on.)

The increased  $Q$  for  $S$  waves may be related to two factors: the decreased percentage of partially molten material or fluid concentration. However, in our case very fast (on the geological time scale) changes in  $Q$  are unambiguous in pointing to a decreasing role of free fluids. Analysis shows that large and great earthquakes are followed by the ascent of fluids from the upper mantle to the crust. This is consistent with the conclusions drawn previously from an analysis of  $S$  wave attenuation field based on the coda of local earthquakes in Tien Shan [10, 12], as well as from the study of time variations in the  $P$  to  $S$  velocity ratio observed in the rupture zone of the 1995 Antofagasta, northern Chile,  $M = 8.0$  earthquake [29]. This is also borne out by the very strong attenuation of  $Lg$  in the rupture zones of large Tien Shan earthquakes inferred from the records of underground nuclear explosions in the Semipalatinsk Test Site [13]. The ascent of juvenile fluids is also corroborated by the presence of mantle helium isotopes in the rupture zones and their near environs [15, 27].

We found a significant dependence of the rate of ascent for mantle fluids on the type of earthquake slip. The abnormally high values of  $Q_1$  and  $Q_1/Q_2$  for great normal and strike-slip earthquakes are consistent with the conclusion that very large volumes of water pour onto the ground surface after large earthquakes having these types of slip in comparison with reverse faulting and thrust earthquakes [32]. The work just referred to shows that normal-slip earthquakes with  $M \sim 7.0$  may be followed by the release of up to  $0.5 \text{ km}^3$  water to the surface. This effect is very probably related to the very high rock permeability in such regions (for strike-slip and reverse-oblique events, although to a lesser degree than is the case for normal faulting mechanisms, one also finds local tension zones (en echelon), where the

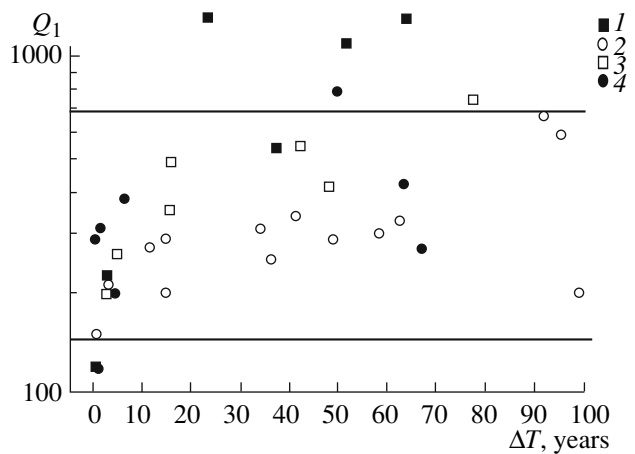


Fig. 12. Dependence of  $Q_1$  on time: (1) normal and normal-oblique faulting, (2) reverse and thrust faulting, (3) reverse-oblique displacement, (4) strike-slip. Horizontal lines enclose the band of data scatter for low seismicity areas.

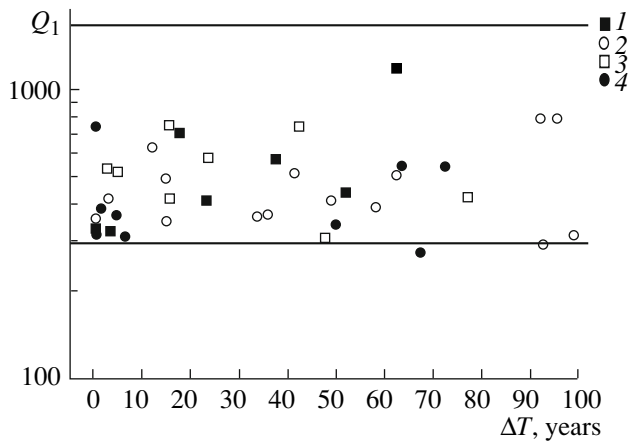


Fig. 13. Dependence of  $Q_2$  on time. For notation see Fig. 12.

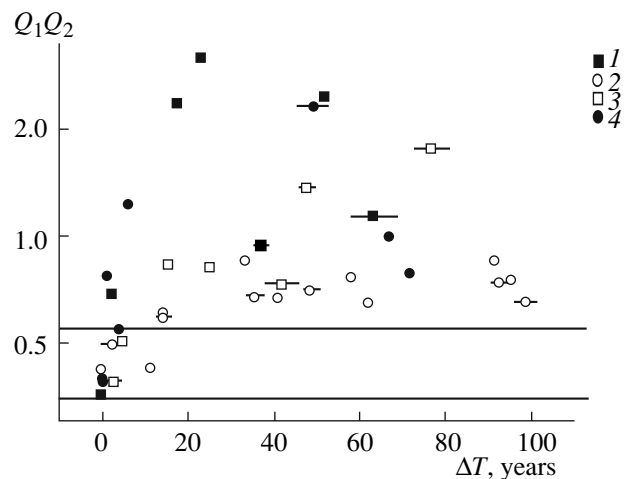
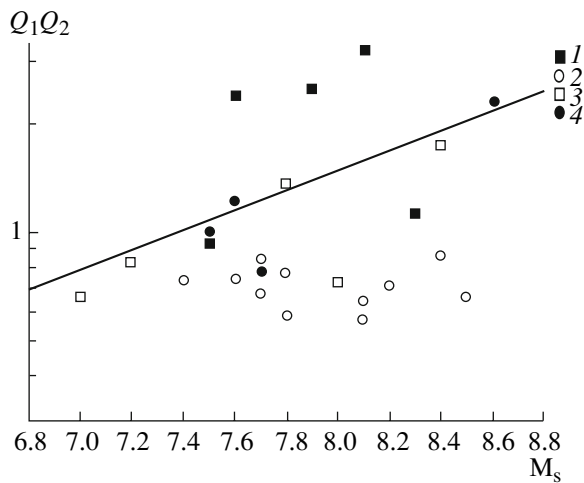


Fig. 14. Dependence of  $Q_1/Q_2$  on time. Horizontal bars are time intervals. For notation see Fig. 12.



**Fig. 15.** Dependence of  $Q_1/Q_2$  on  $M_s$ . Shown is the regression line for normal, normal-oblique, strike-slip, and reverse-oblique faulting. For notation see Fig. 12.

ascent of mantle fluids mostly seems to occur). We note that the existence of such en echelon zones has been found from the coda of local earthquakes occurring in the Racha–Lechkhum right lateral zone in the North Caucasus [1]. At the same time, in compression regions where reverse faulting and thrusting occur, the rock permeability for earthquakes of comparable energy must be much lower (especially for thrust events), which leads to a much lesser “drying” of the upper mantle.

Data obtained for the Assam earthquake zone show that the region where the ascent of mantle fluids is occurring may be much larger than the rupture zone. This is probably related to the fact that fluids may also be migrating laterally into an incipient zone of relative extension [2].

The almost complete absence of time-dependent variations in  $Q_2$  seems to be related to the substantially lower rate of ascent for fluids traveling from greater depths within the upper mantle. At the same time, the very high  $Q_2$  for the rupture zone of the Sanriku-Oki earthquake (1150 as against 270–530, the usual values for the Benioff zones), as well as the decrease in  $Q_1$  and  $Q_1/Q_2$  for normal and strike-slip events for  $\Delta T > 25$  years may indicate that fluids for such types of slip are migrating at greater rates than for reverse and thrust earthquakes from the depth  $\sim > 200$  km, which leads to further diminution of  $Q_1$ .

We note that the lower rate of fluid migration for reverse and thrust earthquakes is consistent with the data obtained earlier for the rupture zones of large Tien Shan earthquakes; the low attenuation in the upper mantle, down to about 200 km, may persist there for at least 100 years after such events [10, 12].

The dependence of  $Q_1/Q_2$  on magnitude for normal, normal-oblique, strike-slip, and reverse-oblique mechanisms can be explained in a natural manner by the

increasing path lengths that the waves must travel in the upper mantle beneath the rupture zone, where the fluids are migrating with increasing energy, and thus, rupture length. The almost complete absence of such a dependence for reverse and thrust events is likely to be due to the fact that the ascent of fluids for such types of slip occurs in local regions, whose sizes are only slightly affected by earthquake energy. Such an effect was previously identified for the rupture zone of the 1889 Chilik earthquake in North Tien Shan [12].

It should be noted that the migration of fluids from the upper mantle is not on the whole questioned by petrologists [18]. It has been previously believed, however, that the ascent is very slow (millions of years). Our data show that fluids can migrate several orders of magnitude faster in the rupture zones of large and great earthquakes. Using the characteristic “drying” time for the upper mantle down to depths of  $\sim 200$ – $250$  km, we find that the rate of ascent for the fluids is of the order of 10 km/yr, or a few tenths of mm/s. This is consistent with our estimates obtained earlier for Tien Shan [12]. We note that S.A. Fedotov found the rate of ascent for viscous magnesia basaltic magma from the crustal boundary as a few cm/s [20], while the average rate of ascent for kimberlite magma within the crust reached values as large as tens of cm/s [17].

It is of interest to note that the ascent of fluids from the upper mantle into the crust can also occur without the occurrence of large earthquakes, as shown by an analysis of deep low-frequency tremors recorded in southwestern Japan [31, 33] where present-day volcanism is absent. In this region the fluids are rising as a result of dehydration of oceanic crustal material in the downgoing Philippine plate.

The specific mechanism that is responsible for the comparatively fast ascent of fluids from the upper mantle is still not clear. We suggest the following hypothesis. In recent years experimental data have been obtained to show that shear stresses can cause significant rearrangements of the fluid field structure; as a result, while originally the fluid was concentrated in the form of isolated bubbles at grain corners, it can now form a connected network propagating along grain boundaries [28, 38]. This must lead to a gradual generation of fluid “domains,” i.e., interconnected channels filled with a liquid phase [26]. When such a domain is sufficiently long vertically, the liquid produces excess pressure to cause a hydraulic fracture at the top of the domain, and the domain rises still higher [2, 26]. As well, large earthquakes themselves and their after-shocks generate powerful vibration excitation in the crust and upper mantle, which may increase the rock permeability by several orders of magnitude [36].

In any case, the ascent of fluids is energetically advantageous, diminishing, as it ultimately does, the Earth’s potential energy. In this respect the effect of earthquakes is like that of volcanic eruptions, which send the liquid phase to the ground surface and release

enormous amounts of volatiles. Obviously, it is no accident that the rupture zones of great crustal earthquakes and volcanoes are far from each other. This is best seen at island arcs, where the ruptures of almost all  $M \geq 8.0$  earthquakes occurring in downgoing oceanic plates are situated at depths shallower than 50 km, while the projections of the volcanoes onto the top of the plates correspond to depths of  $\sim 100$  km or greater [19, 35]. Characteristically, lithospheric plates in plunging into the upper mantle first release the lighter components (fluids) and then denser ones, melts (mostly andesite magmas) [19].

This effect can also be seen on a lesser scale, e.g., in the East African Rift Zone. It is a known fact that the West Rift in that zone has a relatively high seismicity and a very low level of volcanism, while the East Rift shows low seismicity and active volcanic processes [3]. Seismicity and volcanism thus have separated as it were their respective "spheres of influence" as to the ascent of the lighter phase from the mantle.

### CONCLUSIONS

(1) We have studied the characteristics of the short-period shear wave attenuation field in the rupture zones of 37 large and great earthquakes worldwide with  $M_s = 7.0-8.6$ . Their effective  $Q$  was determined from the envelopes of  $Sn$  and  $Lg$  codas in two time intervals ( $Q_1$  and  $Q_2$ ). The quantity  $Q_1$  is a measure of  $S$  wave attenuation in the uppermost mantle down to depths of about 200–250 km, while  $Q_2$  is relevant to deeper horizons of the upper mantle.

(2) It is shown that  $Q_1$  and  $Q_2$  correlate in low seismicity areas, the average ratio being  $Q_1/Q_2 = 0.45 \pm 0.10$ .

(3) The attenuation field in the 1950 Assam earthquake rupture zone has been studied. The values of  $Q_1$  and  $Q_1/Q_2$  found there are very high compared with low seismicity areas.

(4) We have investigated the parameters  $Q_1$ ,  $Q_2$ , and  $Q_1/Q_2$  as functions of the time  $\Delta T$  elapsed after a large earthquake. The parameter  $Q_2$  is almost independent of  $\Delta T$ , while  $Q_1$  and  $Q_1/Q_2$  increase until  $\Delta T \sim 20-25$  years, with the increase being especially pronounced for normal, normal-oblique, and strike-slip earthquake mechanisms.

(5) Our analysis shows that the quality factor of the upper mantle is increasing with time as a large earthquake occurs. This is hypothesized to be related to the ascent of mantle fluids into the crust.

(6) Geodynamic mechanisms were discussed that are thought to be able to bring about a comparatively rapid "drying" of the upper mantle beneath rupture zones.

### ACKNOWLEDGEMENTS

We thank the IRIS DMC for lending us data from the worldwide network of digital GSN stations [24].

### REFERENCES

1. Aptikaeva, O.I., Aref'ev, S.S., Kvetinskii, S.I., et al., Inhomogeneities of the Lithosphere and Asthenosphere in the Rupture Zone of the Racha Earthquake, *Dokl. RAN*, 1995, vol. 344, no. 4, pp. 533–538.
2. Velikhov, E.P., Golubchikov, L.G., and Karakin, A.V., On the Possibility of Using Electrophysical Methods for Prediction and Modification of Shallow Seismicity, *Dokl. RAN*, 2005, vol. 401, no. 2, pp. 238–241.
3. Grachev, A.F., *Riftovye zony Zemli* (Rift Zones of the Earth), Leningrad: Nedra, 1977.
4. Zapol'skii, K.K., Frequency-Selective CHISS Stations, in *Ekspperimental'naya seismologiya* (Experimental Seismology), Moscow: Nauka, 1971, pp. 20–36.
5. Kaazik, P.B., Kopnichev, Yu.F., Nersesov, I.L., and Rakhmatullin, M.Kh., Analysis of the Fine Structure of Short Period Seismic Fields from Array Data, *Fizika Zemli*, 1990, no. 4, pp. 38–49.
6. Kaazik, P.B. and Kopnichev, Yu.F., Numerical Modeling of the  $Sn$  Wave Group and Coda in an Earth with Varying Velocity and Attenuation, *Vulkanol. Seismol.*, 1990, no. 6, pp. 74–87.
7. Kopnichev, Yu.F., *Korotkoperiodnye seismicheskie volnovye polya* (Short Period Seismic Wave Fields), Moscow: Nauka, 1985.
8. Kopnichev, Yu.F. and Arakelyan, A.R., On the Origin of Short Period Seismic Waves at Distances Below 3000 km, *Vulkanol. Seismol.*, 1988, no. 4, pp. 77–92.
9. Kopnichev, Yu.F. and Dyatlikova, I.V., Mapping the Upper Mantle of the Altai–Sayany Region from the Attenuation of Short Period Shear Waves, *Dokl. RAN*, 1990, vol. 312, no. 6, pp. 1348–1351.
10. Kopnichev, Yu.F., Sokolova, I.N., and Shepelev, O.M., Time Variations of the Shear Wave Attenuation Field in the Rupture Zones of Large Tien Shan Earthquakes, *Dokl. RAN*, 2000, vol. 374, no. 1, pp. 99–102.
11. Kopnichev, Yu.F., Pavlis, G., and Sokolova, I.N., Lithospheric Inhomogeneities and the Rupture Zones of Large Earthquakes in Central Tien Shan, *Dokl. RAN*, 2002, vol. 387, no. 4, pp. 528–532.
12. Kopnichev, Yu.F. and Sokolova, I.N., Space–Time Variations of the  $S$  wave Attenuation Field in the Rupture Zones of Large Tien Shan Earthquakes, *Fizika Zemli*, 2003, no. 7, pp. 35–47.
13. Kopnichev, Yu.F. and Sokolova, I.N., Analysis of Space–Time Variations of the Shear Wave Attenuation Field in the Rupture Zones of Large Tien Shan Earthquakes Using Records of Underground Nuclear Explosions, *Dokl. RAN*, 2004, vol. 395, no. 6, pp. 818–821.
14. Kopnichev, Yu.F., Mikhailova, N.N., and Sokolova, I.N., On the Geodynamic Processes in Central Tien Shan: Identification of an Anomalous Region from Seismic Data, *Vestnik NYaTs RK*, 2004, Issue 3, pp. 111–118.
15. Kopnichev, Yu.F. and Sokolova, I.N., The Ascent of Mantle Fluids in the Rupture Zones of Large Earthquakes and in Major Fault Zones: Geochemical Evidence, *Vestnik NYaTs RK*, 2005, Issue 2, pp. 147–155.
16. Kopnichev, Yu.F., Mikhailova, N.N., Sokolova, I.N., and Aristova, I.L., New Evidence Concerning the Geodynamic Processes in the Anomalous Zone of Northern

- Tien Shan: A Possible Precursory Period of a Large Earthquake, *Vestnik NYaTs RK*, 2006, Issue 2, pp. 60–70.
17. Milashev, V.A., *Kimberlity i glubinnaya geologiya* (Kimberlites and Geology of the Interior), Leningrad: Nedra, 1990.
  18. Ringwood, A.E. *Composition and Petrology of the Earth's Mantle*, McGraw-Hill, 1975.
  19. Uyeda, S. *The New View of the Earth: Moving Continents and Moving Oceans*, San Francisco: Freeman, 1978.
  20. Fedotov, S.A., On the Ascent of Basic Magmas in the Earth's Crust and on the Mechanism of Basaltic Fissure Eruptions, *Izv. AN SSSR*, 1976, no. 10, pp. 5–23.
  21. Shchukin, Yu.K., Ryaboi, V.Z., et al., *Glubinnoe stroenie slaboseismichnykh raionov SSSR* (The Deep Structure of Low Seismicity Areas in the USSR), Moscow: Nauka, 1987.
  22. Aptikaeva, O.I. and Kopnichev, Yu.F., Space–Time Variations of Coda Wave Envelopes of Local Earthquakes in Central Asia, *J. Earthq. Predict. Res.*, 1993, vol. 2, no. 4, pp. 497–514.
  23. Burford, R. and Harsh, P., Slip on the San Andreas Fault in Central California from Alinement Array Surveys, *Bull. Seismol. Soc. Amer.*, 1980, vol. 70, no. 4, pp. 1233–1261.
  24. Butler, R., Lay, T., Creager, K., et al., The Global Seismographic Network Surpasses Its Design Goal, *EOS Transactions AGU*, 2004, vol. 85, no. 23, pp. 225–229.
  25. Chen, W.-P. and Molnar, P., Seismic Moments of Major Earthquakes and Average Rate of Slip in Central Asia, *J. Geophys. Res.*, 1977, vol. 82, no. 20, pp. 2945–2969.
  26. Gold, T. and Soter, S., Fluid Ascent through the Solid Lithosphere and Its Relation to Earthquakes, *PAGEOPH*, 1984/1985, vol. 122, pp. 492–530.
  27. Güleç, N., Hilton, D., and Mutlu, H., Helium Isotope Variations in Turkey: Relationship to Tectonics, Volcanism and Recent Seismic Activities, *Chem. Geol.*, 2002, vol. 187, pp. 129–142.
  28. Hier-Majumder, S. and Kohlstedt, D., Role of Dynamic Grain Boundary Wetting in Fluid Circulation beneath Volcanic Arcs, *Geophys. Res. Lett.*, 2006, vol. 33, L08305.
  29. Husen, S. and Kissling, E., Postseismic Fluid Flow after the Large Subduction Earthquake of Antofagasta, Chile, *Geology*, 2001, vol. 29, no. 9, pp. 847–850.
  30. McNamara, D., Owens, T., and Walter, W., Observations of Regional Phase Propagation across the Tibetan Plateau, *J. Geophys. Res.*, 1995, vol. 100, no. B11, pp. 22 215–22 229.
  31. Miyazawa, M. and Mori, J., Evidence Suggesting Fluid Flow beneath Japan Due to Periodic Seismic Triggering from the 2004 Sumatra–Andaman Earthquake, *Geophys. Res. Lett.*, 2006, vol. 33, L05303.
  32. Muir-Wood, R. and King, G., Hydrological Signatures of Earthquake Strain, *J. Geophys. Res.*, 1993, vol. 98, no. B9, pp. 15 779–15 795.
  33. Obara, K., Nonvolcanic Deep Tremors Associated with Subduction in Southwest Japan, *Science*, vol. 296, pp. 1679–1681.
  34. Pacheko, J. and Sykes, L., Seismic Moment Catalog of Large Shallow Earthquakes, 1900 to 1989, *Bull. Seismol. Soc. Amer.*, 1992, vol. 82, no. 3, pp. 1306–1349.
  35. Peacock, S. and Hyndman, R., Hydrous Minerals in the Mantle Wedge and the Maximum Depth of Subduction Thrust Earthquakes, *Geophys. Res. Lett.*, 1999, vol. 26, no. 16, pp. 2517–2520.
  36. Rojstachzer, S. and Wolf, S., Permeability Changes Associated with Large Earthquakes: An Example from Loma Prieta, California, *Geology*, 1992, vol. 20, pp. 211–214.
  37. Sato, H. and Fehler, M., *Seismic Wave Propagation and Scattering in the Heterogeneous Earth*, New York: Springer-Verlag Inc., 1998.
  38. Takei, Ya., Deformation-Induced Grain Boundary Wetting and Its Effects on the Acoustic and Rheological Properties of Partially Molten Rock Analogue, *J. Geophys. Res.*, 2005, vol. 110, no. B12, B12203.
  39. Triep, E. and Sykes, L., Frequency of Occurrence of Moderate to Great Earthquakes in Intracontinental Regions: Implications for Changes in Stress, Earthquake Prediction, and Hazards Assessments, *J. Geophys. Res.*, 1997, vol. 102, no. B5, pp. 9923–9948.